Nanoscale Advances

ROYAL SOCIETY OF CHEMISTRY

PAPER

View Article Online
View Journal | View Issue

Cite this: *Nanoscale Adv.*, 2025, **7**, 3881

A simple, scalable protocol for the synthesis of ricinoleic acid-functionalised superparamagnetic nanoparticles with tunable size, shape, and hydrophobic or hydrophilic properties†

Sohel Reja *

Vegetable oils such as oleic acid have been widely used in the synthesis of nanomaterials as they are environmentally benign, cheap, and biodegradable. Ricinoleic acid (RA), which differs from oleic acid by the presence of an additional hydroxyl group, has surprisingly remained unexplored in the preparation of metal oxide nanoparticles, although it offers the advantage over oleic acid of easy functionalization due to the presence of the hydroxyl group. Here is a simple one-pot procedure for the synthesis of a variety of superparamagnetic nanoparticles, iron oxides and ferrites, using RA both as a precursor complexing agent and as a capping agent outlined. This procedure overcomes the challenges associated with the traditional thermal decomposition method, which demands separate precursor preparation and purification steps, thus promoting a simple yet scalable economic production of various magnetic nanoparticles. Minor changes in the reaction conditions allowed for the production of nanoparticles with different sizes, ranging from 5 to 17 nm, as well as different shapes, spherical and cuboid. Iron oxide nanospheres with an average particle size of 10 nm were superparamagnetic at room temperature with a saturation magnetization of 41 emu g^{-1}. The as-prepared RA-coated nanoparticles are hydrophobic and dispersible in non-polar solvents but may easily be rendered hydrophilic and water dispersible; epoxidation, followed by alkaline ring-opening, produced hydroxylated nanoparticles with a positive zeta potential of 31 eV, whereas exchange of the capping RA with nitrilotriacetic acid (NTA) gave nanoparticles with a negative zeta potential of −25 eV. The present study highlights the uniqueness of using RA in the preparation of magnetic nanoparticles; apart from the ease and economics of scaling, it offers the possibility of the nanoparticles being either hydrophobic or hydrophilic.

Received 13th February 2025
Accepted 5th May 2025

DOI: 10.1039/d5na00150a

rsc.li/nanoscale-advances

Introduction

In an era where nanomaterials have established a significant foothold in almost every aspect of modern science, the long-term environmental impact of the hazardous chemicals used as precursors in their synthesis has been a cause of concern.[1–3] Vegetable oils, primarily composed of long-chain fatty acids, are excellent choices as they are environmentally benign, cheap, biodegradable, and biocompatible.[4] Oleic acid (OA), an 18-carbon unsaturated fatty acid, has been extensively studied in the synthesis of metal oxide nanoparticles with precise size and shape tunability.[5–7] Here, we demonstrate the use of ricinoleic acid (RA) that differs from oleic acid by the presence of an additional hydroxyl group at the C12 position (ESI, Fig. S1†) in the preparation of superparamagnetic iron oxide nanoparticles (SPIONS). RA is obtained from castor oil; it constitutes 90% of the total fatty acid content and is extracted by saponification.[4,8–10] The use of RA in nanomaterial synthesis can, in principle, offer multiple advantages over OA, which is currently widely used. While the long aliphatic tail imparts ready solubility in non-polar solvents, the presence of the hydroxyl group allows for moderate solubility in relatively polar solvents.[4] The presence of the hydroxyl group would allow for further functionalization of the nanoparticle surface, for example, acetylation and polymerization.[4] Despite the immense popularity of OA in nanoparticle synthesis, the use of the structurally similar RA has remained vastly unexplored.[8]

Synthetic protocols for the preparation of nanoparticles usually employ a 'capping agent' to modulate particle morphology and dimensions as well as to prevent aggregation. Capping agents such as trioctylphosphine (TOP) and trioctylphosphine oxide (TOPO) are widely used in the preparation of metal oxides and metal chalcogenide semiconductor nanoparticles. The severe toxicity, as well as their pyrophoric and explosive nature, is, however, a major impediment to their

Department of Inorganic and Physical Chemistry, Indian Institute of Science, Bangalore, Karnataka 560012, India. E-mail: sohelreja@iisc.ac.in

† Electronic supplementary information (ESI) available. See DOI: https://doi.org/10.1039/d5na00150a

usage.[4] The use of RA as a capping agent offers a greener alternative.[4,11] The presence of RA on the nanoparticle surface not only imparts excellent colloidal stability but also offers reactive functionalities for oxidation, acetylation and polymerization reactions.[4,10,12,13] Ricinoleic acid functionalized upconversion nanoparticles have been prepared following solvothermal[14] and thermal decomposition methods; subsequent hydroxylation produced nanoparticles that were readily dispersible in water.[15] In another study, the ready reactivity of the hydrothermally prepared RA-coated upconversion nanoparticles was demonstrated by reaction with dodecanoyl chloride.[14] The hydroxyl group of the RA-coated iron oxide nanoparticles has been exploited to initiate the ring-opening polymerization of polylactic acid.[16] Despite the rich surface chemistry offered by RA, it has been less widely investigated.

A diverse range of synthetic protocols are available for the synthesis of SPIONS and ferrite nanoparticles. Of these, thermal decomposition has been the frontrunner as it produces size and shape-tunable monodisperse nanoparticles with the scope of scaling up and further functionalization.[6,17,18] The popular precursor choices are iron acetylacetonate, iron pentacarbonyl, and iron oxyhydroxide. Irrespective of the choice of the starting precursor, iron oleate itself takes part in the actual thermal decomposition process.[19] Organometallic precursors such as iron pentacarbonyl require special treatments because of their sensitivity, flammability and toxicity, thus making them economically unviable for commercial production.[20] Iron acetylacetonate, although a less expensive precursor, often requires benzylated solvents and reducing agents in the preparation process. The acetylacetone formed as a result of early decomposition of iron acetylacetonate must be thoroughly removed from the reaction mixture to ensure monodispersity in particle size distribution.[21] Preparation of iron oxyhydroxide requires treating iron salt in a highly basic medium. The product precursor requires thorough washing and drying.[22] Iron oleate is perhaps the most popular and widely investigated precursor for the production of SPIONs. The additional precursor synthesis, separation, and purification steps, however, add to the production cost.[20] Hydrated iron oleate often produces polydisperse nanoparticles.[23–25] Following the thermal decomposition route, the synthesis of single-component iron oxide may sound promising, but the synthesis of binary or ternary ferrites, which are multi-component mixed-metal oxides, may become challenging.

An efficient single-pot preparation method that avoids the use of expensive and environment-sensitive precursors and avoids demanding precursor preparation steps will not only simplify the nanoparticle synthesis process in terms of cost-efficiency and scalability but also boost batch reproducibility.[8,26] In this study, RA was employed in the synthesis of SPIONs. RA functions both as a metal-complexing and capping agent. It is shown here that hydroxylation of the surface-attached ricinolate can render the particles hydrophilic and readily dispersible in water. Additionally, an easy and efficient phase-transfer protocol to render the hydrophobic RA-coated nanoparticles hydrophilic using trisodium nitrilotriacetate (NTA), a popular chelating agent that possesses multiple carboxyl groups, is outlined.

Experimental section

Materials

Ferric nitrate nonahydrate ($Fe(NO_3)_3 \cdot 9H_2O$), manganese nitrate hexahydrate ($Mn(NO_3)_2 \cdot 6H_2O$), cobalt nitrate hexahydrate ($Co(NO_3)_2 \cdot 6H_2O$), isopropanol, acetone, *n*-hexane, formic acid, hydrogen peroxide (30%) chloromethane, and chloroform were purchased from SD Fine Chemicals. Sigma-Aldrich provided trisodium nitrilotriacetate monohydrate ($Na_3NTA \cdot H_2O$) and 1-octadecene. All chemicals were used as received without further purification. Ricinoleic acid (RA) and sodium ricinoleate were purchased from TCI Chemicals. All chemicals were used without further purification.

Synthesis of iron oxide nanospheres. In a typical synthesis of ricinoleic acid-coated superparamagnetic iron oxide nanoparticles (RA@SPIONs), 2 mmol $Fe(NO_3)_3 \cdot 9H_2O$ was added to 30 mL of isopropanol and 8 mL of 1-octadecene in a round-bottom flask with continuous stirring. The red-brown solution was heated to 150 °C for 30 minutes, followed by the addition of 12 mmol of RA. The solution was refluxed at 320 °C for 2 hours under an inert atmosphere. During the reaction, the solution changed colour from dark brown to black. The system was left to cool, and subsequently, 30 mL of a 2 : 1 mixture of acetone and chloroform was added to precipitate the iron oxide nanocrystals. The precipitate was separated by centrifugation at 7000 rpm for 5 minutes. The washing steps were repeated three times, followed by a single wash with 30 mL acetone to remove excess RA and octadecene. The product was subsequently dried at 60 °C overnight. The synthesis was repeated on a 15× scale to verify the scalability.

Synthesis of ultrasmall iron oxide nanoparticles. Ultrasmall iron oxide nanoparticles were obtained by replacing RA with a mixture of 8 mmol of oleyl alcohol and 8 mmol of RA. The rest of the procedure remained the same as nanosphere synthesis.

Synthesis of iron oxide nanocuboids. Cuboid iron oxide nanoparticles were obtained by replacing RA with 2 mmol of sodium ricinolate and 8 mmol of RA. During product purification, thorough washing with ethanol was necessary to separate the nanoparticles from the viscous tar-like product.

Synthesis of ferrite nanoparticles. In a typical synthesis of $MnFe_2O_4$, 2 mmol $Fe(NO_3)_3 \cdot 9H_2O$ and 1 mmol $Mn(NO_3)_2 \cdot 6H_2O$ were added to 45 mL of isopropanol and 12 mL of 1-octadecene in a round-bottom flask with stirring. The red-brown solution was heated to 150 °C for 30 minutes, followed by the addition of 18 mmol of RA. The rest of the procedure remained the same as that of iron oxide nanoparticles. For the preparation of $CoMnFe_2O_4$ ferrite nanoparticles, a 2 : 0.5 : 0.5 molar mixture of $Fe(NO_3)_3 \cdot 9H_2O$, $Mn(NO_3)_2 \cdot 6H_2O$ and $Co(NO_3)_2 \cdot 6H_2O$ was taken. For the synthesis of ferrite nanocuboids, RA was replaced with 3 mmol sodium ricinolate and 12 mmol RA. The rest of the procedure remained the same.

Aliquots were collected at an intermediate stage to study the formation of precursor ricinolate complexes with infrared spectroscopy. In the preparation of iron oxide nanoparticles, for

instance, following the addition of RA, the reaction mixture was aged for 30 minutes before collecting the aliquot (Fe-RA). Similarly, manganese ricinolate (Mn-RA) and iron-manganese ricinolate (Fe–Mn-RA) precursor complex aliquots were collected.

Hydroxylation of RA@SPIONs (OH@SPIONs). For the hydroxylation of RA@SPIONs, 10 mg of RA@SPIONs were ultrasonically dispersed in 5 mL of chloromethane. Subsequently, 0.1 mL of formic acid was added to the dispersion immersed in an ice bath, followed by an equal volume of 30% H_2O_2. The reaction continued for 6 hours at room temperature. The product was separated magnetically. Subsequently, 10 mL of 1 N NaOH was added and ultrasonicated for five minutes in a bath sonicator, followed by vigorous magnetic stirring for an hour. The product was separated magnetically, washed with ethanol, acetone, and water, and then dried overnight in a hot-air oven.

NTA functionalization of RA@SPIONs (NTA@SPIONs). For the direct phase transfer of the nanocrystals, the reaction mixture containing RA-capped iron oxide nanoparticles in octadecene was cooled to room temperature. Subsequently, 20 mmol of NTA in 30 mL of water/ethanol (1 : 2 v/v) and 10 mL of toluene were added to the reaction mixture and vigorously stirred for 4 hours at 80 °C. After that, the product was separated from the reaction mixture with a handheld bar magnet. Subsequently, the product was redispersed in 30 mL ethanol, followed by centrifugation at 7000 rpm for 5 minutes. The washing steps were repeated with acetone and water. The as-produced nanoparticles were readily dispersible in water.

Characterization

The phase composition of the nanocrystals was determined using a PANalytical Empyrean X-ray diffractometer (XRD) equipped with a Pixel 3D detector with Cu Ka radiation under flat-stage configuration and Gonio scan axis settings. The measurements were recorded in the 2θ range of 25 to 67° with a step size of 0.062606° and time per step of 500 seconds. The product powder (~20 mg) was placed on a glass plate for the measurements. The size and shape evolution of the nanocrystals were studied with a JEOL JEM 2100 F transmission electron microscope (TEM), operated at an acceleration voltage of 200 kV with a Tungsten–Zirconium oxide field emission electron source. For preparing TEM samples, hexane dispersions of the nanoparticles were drop-coated on the CF300 TEM grids, followed by overnight vacuum drying. Magnetic properties were measured with a Quantum Designs PPMS 9T 639. For isothermal (300 K) M–H measurements, 5–10 mg of powder samples were packed with Teflon strips. A Bruker ALPHA-II Compact ATR (Attenuated Total Internal Reflectance) was used to record infrared spectra (IR) of the powder samples. A Malvern Zetasizer ZS has been used for zeta potential and dynamic light scattering (DLS) studies. The samples were prepared by ultrasonicating 1 mg mL^{-1} nanoparticle dispersion in water, followed by centrifugation at 3000 rpm for 3 minutes. Elemental analysis was done with a Thermo Fisher Scientific X-ray photoelectron spectrometer (XPS) with pass energy: 50 eV, dwell time: 50 ms and energy step size: 0.1 eV. The samples were prepared by drop coating 1 mg mL^{-1} nanoparticle dispersion on silicon wafers, followed by overnight vacuum drying.

Results and discussion

A facile one-pot thermal decomposition route was adopted for the preparation of SPIONs with shape and size tunability (Scheme 1a).[20] Traditional thermal processes for nanoparticle synthesis involve the synthesis of metal-fatty acid complexes, such as metal oleate for oleic acid-coated nanoparticles, as a separate and complicated step. These additional steps are time-consuming and can produce hydrated precursors.[23] While oleic acid has received extensive attention, ricinoleic acid (RA) has not been probed much in the synthesis of superparamagnetic iron oxide and ferrite nanoparticles. In this work, we offer a simplified approach using RA as both a metal-complexing and nanoparticle capping agent that allows *in situ* precursor formation and eliminates the need for complicated separate precursor preparation steps. The preparative procedure allowed for the scaled-up production of SPIONs on a gram scale and could be extended for the preparation of ferrite nanoparticles with spherical and cuboid morphology. Alcoholic hydrolysis of iron nitrate into iron hydroxide and subsequent *in situ* precursor oleate complex formation had been explored in a previous study.[20] In this work, oleic acid is replaced with RA.

Assuming the complete dissolution of the iron nitrate in alcohol, the following equilibrium occurs in the solution.

$$Fe^{3+} + 3OH^- \rightleftharpoons Fe(OH)_3$$

The undisturbed alcoholic solution of iron nitrate turns turbid as the iron hydroxide precipitates out of the reaction medium. When heated to 150 °C, the appearance of brown fume indicated the decomposition of nitrates into oxides of nitrogen. With the further addition of RA, iron hydroxide forms the precursor iron ricinolate complex. At elevated temperatures, the precursor ricinolate complex decomposes to produce iron

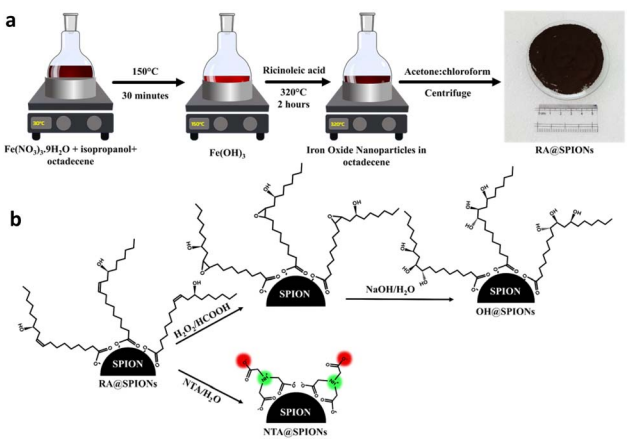

Scheme 1 Schematic representation of the (a) synthesis and (b) surface functionalization RA@SPIONs.

oxide nanocrystals. The size of the spherical nanoparticles was controlled by varying the reaction time. For producing cubic nanoparticles, RA was replaced with a mixture of RA and sodium ricinolate. Ultrasmall iron oxide nanoparticles (5 nm) were prepared by replacing RA with a mixture of RA and oleyl alcohol. Subsequent hydroxylation of the nanoparticles (Scheme 1b) produced water-dispersible nanoparticles which were positively charged. NTA-mediated phase transfer, on the other hand, produced zwitterion-coated SPIONs, which showed good colloidal stability in aqueous dispersions.

The formation of the precursor ricinolate complex was confirmed from the infrared spectrum (IR) (Fig. 1a). The appearance of the asymmetric (1560–1600 cm^{-1}) and symmetric (1400–1430 cm^{-1}) carboxylate stretching bands in the infrared spectra of manganese ricinolate, iron ricinolate, and the manganese-iron ricinolate confirms the successful formation of the metal ricinolate complexes. The presence of the carboxylate stretching bands at 1433 and 1543 cm^{-1}, as well as the methyl stretching mode at 2863 and 2940 cm^{-1} in the infrared spectra of the RA@SPIONs (Fig. 1b), indicates the presence of ricinolate groups as capping agents on the nanoparticle surface. The presence of long hydrocarbon tails of the surface-bound RAs renders the nanoparticles ready for dispersibility in non-polar solvents such as cyclohexane, chloroform and toluene.

The powder X-ray diffraction (PXRD) pattern of the iron oxide nanoparticles is shown in Fig. 1c. Distinguishing the crystal phase of iron oxide based on PXRD is challenging since two cubic spinel iron oxide phases, magnetite and maghemite, produce very similar PXRD patterns. Rietveld analysis of the diffraction pattern produced the best with a phase combination of 64.6% magnetite (Fe_3O_4; ref no: 96-900-5840) and 35.4% maghemite (γ-Fe_2O_3; ref no: 96-900-6316), rather than a single component (magnetite or maghemite).

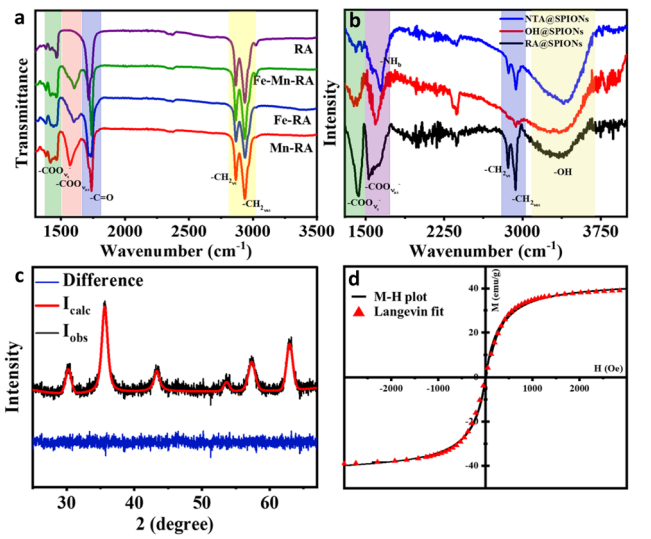

Fig. 1 (a) Infrared spectra of RA (RA), manganese ricinolate (Mn-RA), iron ricinolate (Fe-RA), and iron-manganese ricinolate (Fe–Mn-RA). (b) Infrared spectrum of RA@SPIONs, NTA@SPIONs and OH@SPIONs. (c) PXRD of RA@SPIONs. The red line represents the best fit from Rietveld analysis with a magnetite and maghemite phase mixture. The difference is shown in blue. (d) Isothermal (300 K) magnetization (M–H) curve (in bold line) and corresponding Langevin fitting (red squares) for the RA@SPIONs.

The isothermal magnetization (M) as a function of the applied magnetic field (H) for the RA@SPIONs was measured at room temperature (300 K) (Fig. 1d). The M–H plot passes through the origin with zero remanence and coercivity, indicating the single-domain nature of the nanoparticles. A modified Langevin equation was fitted to confirm the superparamagnetic nature of the nanocrystals.[20]

$$M = M_0 L(x) + \chi H$$

where $L(x) = [\coth(x) - (1/x)]$ is the Langevin function, M is the magnetic moment, H is the applied magnetic field, M_0 is the saturation magnetization, and $x = \mu_p H/k_B T$, where μ_p is the particle magnetic moment, k_B is the Boltzmann constant, T is the absolute temperature, and χ is the susceptibility of the ferrimagnetic nanoparticles, as predicted by Néel for particles with antiferromagnetic interactions. A saturation magnetization of 41.3 emu g^{-1} was obtained from the Langevin fitting parameters. The significantly reduced magnetization compared to the bulk (82 emu g^{-1}) could be because of the reduced particle size as well as the presence of a 'magnetic dead layer' on the nanoparticle surface.[27]

In the thermogravimetric analysis (TGA) plot of the iron ricinolate complex (ESI, Fig. S2a†), the first mass loss in the temperature range of 280–360 °C may be due to the decomposition of the free or loosely bound RA, whereas the second mass loss in the temperature range of 380–470 °C may be attributed to the decomposition of the metal–ricinolate complex. In the TGA plot of RA@SPIONs, the mass loss in the range of 300–460 °C may be due to the decomposition of the surface-bound RA (ESI, Fig. S2b†).[8,28]

The transmission electron microscopy (TEM) image of the RA@SPIONs is shown in Fig. 2a. The average particle size was 10 nm. The result is in good agreement with the crystallite size estimated from the PXRD using the Debye–Scherrer equation (9 nm). The selected area electron diffraction (SAED) shows bright spots that could be indexed to the (220), (311), (400), (511), and (440) planes of the cuboid iron oxide (ESI, Fig. S3†). The TEM image showed particles with contrast variation, which may be attributed to the difference in particle thickness and zone axes. A high-resolution TEM (HRTEM) image of the light and dark particles is shown in Fig. 2b and c. Particles with lighter contrast (Fig. 1b) show lattice fringes with the characteristic spacings of the (311) and (400) planes of spinel iron oxide, as confirmed by the Fast Fourier Transform (FFT) (Fig. 2b inset). Particles with darker contrast (Fig. 2c) show lattice fringes corresponding to the (311) and (220) planes of spinel iron oxide. The bright spots in the FFT may be assigned to the (311) and (220) planes of spinel iron oxide (Fig. 2c inset).

Tunability of the nanoparticle size and shape is an important aspect of the synthesis protocol adopted. Iron oxide nanoparticles with an average size of 17 nm were produced when the reaction time was extended to 4 hours (Fig. 3c). Formation of larger nanoparticles with increasing reaction time may be due

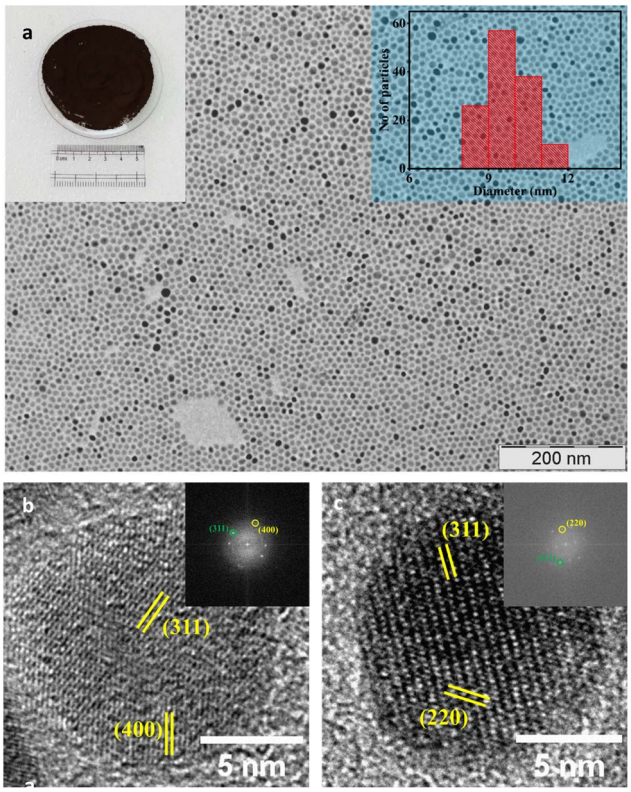

Fig. 2 (a) TEM image of RA@SPIONs produced on a large scale. The inset to the left shows a photograph of iron oxide nanoparticles produced from a single batch. The inset to the right shows the particle size histogram. Indexed HRTEM and corresponding FFT of a particle with (b) lighter and (c) darker contrast.

to the extended growth phase, which favours Ostwald's ripening.[20] For obtaining ultrasmall iron oxide nanoparticles (5 nm), a surfactant mixture comprising RA and oleyl alcohol was used (Fig. 3a). Oleyl alcohol, a mild reducing agent, lowers the decomposition temperature of the precursor iron ricinolate complex, which results in the formation of a large number of nuclei, ultimately resulting in smaller nanoparticles.[29] The considerably reduced saturation magnetization for the ultrasmall iron oxide nanoparticles, 19 emu/g, may be due to a significant contribution from the magnetic dead layer (ESI, Fig. S4†).[27]

Cuboid RA@SPIONs could be obtained by employing a surfactant mixture of RA and sodium ricinolate (Fig. 3d). Sodium ricinolate promotes preferential adhesion to the {100} facets of the iron oxide crystals during the growth phase. The slower growth rate of the {100} plane ultimately results in the cube formation.[30–32] The ultrasmall and cubic iron oxide nanoparticles show Bragg reflections corresponding to the cubic spinel phase (space group: $Fd\bar{3}m$) of iron oxide as supported by PXRD (ESI, Fig. S5†).

The modified thermal decomposition route was adopted for the synthesis of binary and ternary ferrite nanoparticles.[33–35] The Bragg reflections in the PXRD pattern of $MnFe_2O_4$ and $CoMnFe_2O_4$ nanospheres and nanocuboids may be indexed to the (220), (311), (400), (511), and (440) planes of the cuboid spinel phase (ESI, Fig S5†). The TEM images of the $MnFe_2O_4$ and $CoMnFe_2O_4$ nanospheres and nanocuboids are shown in Fig. 4. The lattice fringes in the HRTEM of the $MnFe_2O_4$ and $CoMnFe_2O_4$ can be indexed to the cubic ferrite phase (ESI, Fig. S6†). In the high-resolution X-ray photoelectron spectrometer (XPS) spectra of $CoMnFe_2O_4$, the Mn, Co, and Fe $2p_{3/2}$ and $2p_{1/2}$ peak positions are characteristic of M^{2+} (M = Mn, Co) and Fe^{3+} oxidation states, respectively (ESI, Fig. S7†). The skewed nature of the peaks may be due to the contribution from additional oxidation states of the metal cations.[36,37] The binding energies of the elements are given in Table S1† of the ESI.† The $MnFe_2O_4$ nanospheres were superparamagnetic, as confirmed by the Langevin fitting, and the saturation magnetization was 39 emu/g (ESI, Fig. S4†).

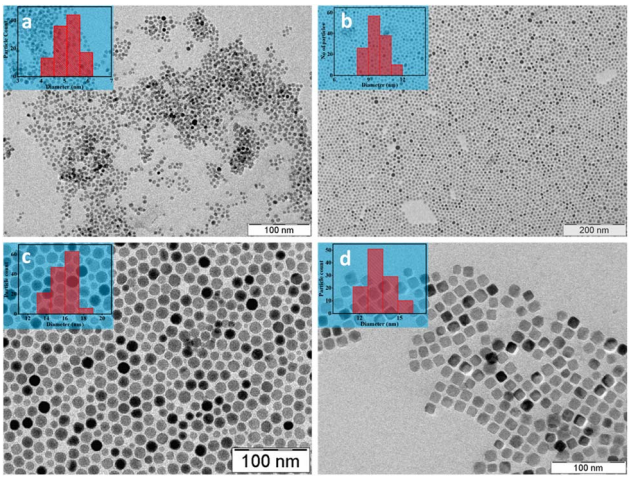

Fig. 3 TEM images of RA@SPIONs with an average size of (a) 5 nm, (b) 10 nm, and (c) 17 nm. (d) TEM image of nanocuboid RA@SPIONs. The inset shows the particle size histogram.

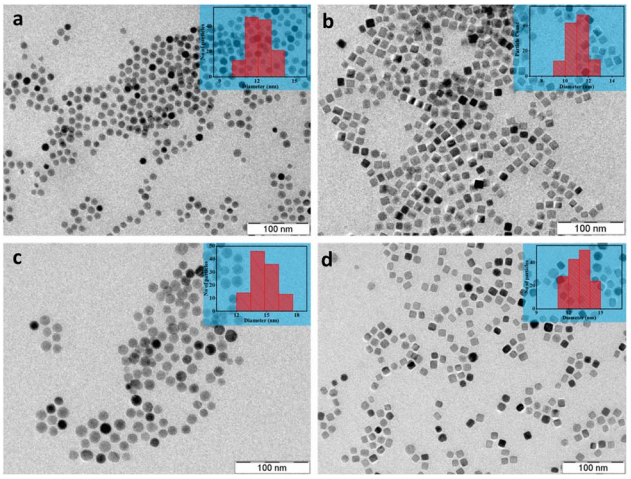

Fig. 4 TEM images of $MnFe_2O_4$ (a) nanospheres and (b) nanocuboids. TEM images of $CoMnFe_2O_4$ (c) nanospheres and (d) nanocuboids. The inset shows the particle size histogram.

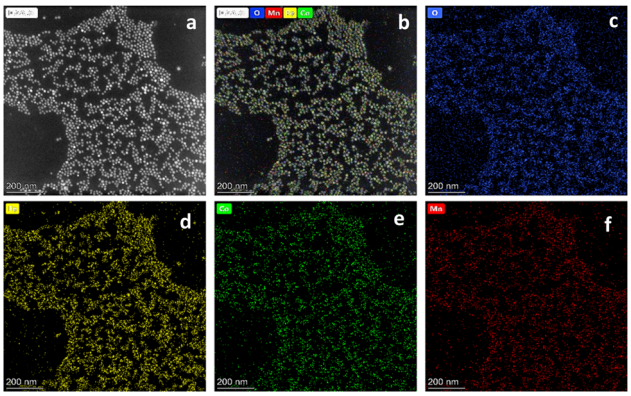

Fig. 5 EDS colour mapping of the $CoMnFe_2O_4$ nanoparticles. (a) HAADF, (b) overlapped, (c) O, (d) Fe, (e) Co and (f) Mn.

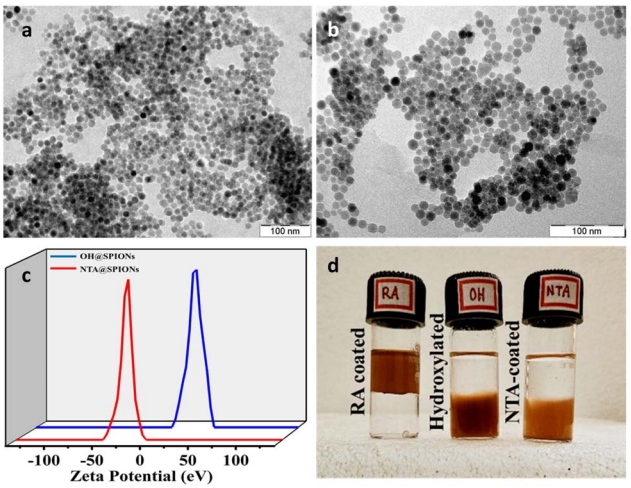

Fig. 6 TEM images of (a) NTA@SPIONs and (b) OH@SPIONs. (c) The zeta potential of the NTA@SPIONs and OH@SPIONs at pH 7, and (d) a photograph showing the colloidal dispersions of the RA@SPIONs, NTA@SPIONs and OH@SPIONs in a 1 : 1 solvent mixture of water and toluene.

The energy dispersive spectroscopy (EDS) mapping of the $CoMnFe_2O_4$ is shown in Fig. 5. The uniformity in the cation distribution over the nanoparticles indicates the presence of a homogeneous unitary ferrite phase. Similarly, in the EDS spectra of $MnFe_2O_4$ nanoparticles, the uniform distribution of Mn^{2+} and Fe^{3+} indicates the homogeneity in the elemental composition of the nanoparticles (ESI, Fig. S8†).

Surface engineering of nanomaterials is a research domain as critical as the synthesis itself. Surface-attached ricinolate not only imparts chemical stability to the iron oxide core but also renders the nanoparticles hydrophobic and, thus, readily dispersible in non-polar solvents. However, to transfer the nanoparticles to an aqueous medium, ligand modifications are necessary (Fig. 6d). Different strategies were adopted for the surface functionalisation of the RA@SPIONs- (a) ligand modification and (b) ligand exchange (Scheme 1b). Ligand exchange with zwitterionic NTA resulted in pH-responsive charge switchable magnetic nanoparticles, which may be exploited for selective adsorption of oppositely charged target molecules.[38] Chemically modifying the ligand, on the other hand, produced hydroxylated nanoparticles, which not only imparted good colloidal stability in water but may also facilitate further functionalisation through the labile hydroxyl groups.

The ligand modification of the RA@SPIONs was achieved by epoxidation of the unsaturation present in the ricinolate backbone with H_2O_2/HCOOH, followed by base-mediated (NaOH/H_2O) ring opening of the epoxide to form hydroxylated SPIONs. In the infrared spectrum of the OH@SPIONs (Fig. 1b), the broad peak in the range of 3350–3600 cm^{-1}, characteristics of –OH stretching, is pronounced compared to RA@SPIONs. Additionally, the vibrational band at 1600 cm^{-1}, characteristic of –OH bending, is also intense, which indicates an increase in the number of surface hydroxyl groups post-functionalization (Fig. 1b). The presence of the hydroxyl groups on the nanoparticle surface makes the nanoparticles water-dispersible (Fig. 6d). The zeta potential study indicates that the particles are positively charged (31 eV) (Fig. 6c). The dynamic light scattering (DLS) measurement showed a unimodal distribution with an average hydrodynamic diameter of 42 nm (ESI, Fig. S9†). In the TEM image of the OH@SPIONs (Fig. 6b), slight aggregation is noted, which may be attributed to the interparticle H-bonding.

The NTA@SPIONSs were also rendered hydrophilic by a ligand exchange-mediated phase transfer using NTA, an aminopolycarboxylate. The use of NTA in nanoparticle phase transfer had been explored in a previous report. In the infrared spectrum of the NTA@SPIONs (Fig. 1b), the peak at 1645 cm^{-1} can be attributed to the -$NH_{bending}$ of the surface-attached NTA groups (Fig. 1b).[38] NTA@SPIONs are zwitterionic in nature with an isoelectric point at pH 5.1.[38] At pH 7, the nanoparticles are negatively charged, as is evident from the zeta potential measurements (−25 eV) (Fig. 6c). The particles displayed good colloidal dispersibility without any aggregation. The DLS measurements showed a unimodal number-weighted hydrodynamic diameter distribution (ESI, Fig. S9†) with an average hydrodynamic diameter of 29 and 38 nm for the OH@SPIONs and NTA@SPIONs, respectively. The TEM image of the NTA@SPIONs is shown in Fig. 6a. The aggregation of the nanoparticles in the TEM image may be due to the surface carboxylates, which, apart from being much shorter than the ricinolate chains, may be involved in intraparticle H-bonding.

Conclusion

Superparamagnetic nanoparticles are of current interest in the fields of MRI contrast agents, targeted drug delivery, magnetic hyperthermia, catalysis and magnetic adsorbents for wastewater remediation. Traditionally, oleic acid has been used both as a precursor and a capping agent in the preparation of nanomaterials. In the present study, the use of RA to prepare superparamagnetic nanoparticles of iron oxides and transition metal ferrites has been explored. RA, which constitutes 90% of the total fatty acid content in castor oil, has all the attributes of oleic acid but additionally has the advantage of easy

functionalization due to the presence of the hydroxyl group at the C12 position. A simple one-pot scheme wherein RA is both the precursor complexing agent and the capping agent has been developed. This method overcomes the challenges associated with the traditional thermal decomposition route by avoiding separate steps for the preparation of the precursor and its purification, making the process scalable and low-cost. A general synthetic protocol using this method for producing a variety of magnetic nanoparticles, iron oxides, and ferrites is outlined. The method produces nanoparticles with a narrow, almost monodisperse distribution. Minor modifications in the preparation scheme allow for precise control of particle dimensions, from 5 to 17 nm, as well as morphologies, either spheroid or cuboid. Iron oxide nanoparticles obtained by this method showed the presence of both magnetite and maghemite phases. The particles are superparamagnetic at room temperature with a saturation magnetization of 41 emu g^{-1}. The as-prepared nanoparticles are hydrophobic and dispersible in non-polar solvents but may easily be rendered hydrophilic by hydroxylation of the capping RA to give stable aqueous dispersions with a positive zeta potential (+31 eV). Alternatively, hydrophilic magnetic nanoparticles could be obtained by exchanging the capping ligand RA with nitrilotriacetic acid (NTA). The NTA-capped magnetic nanoparticles also formed a stable aqueous dispersion, but with a negative zeta potential (−25 eV). The present study highlights the uniqueness of using RA in the preparation of magnetic nanoparticles; apart from the ease and economics of scaling, it offers the possibility of the nanoparticles being either hydrophobic or hydrophilic, thereby greatly extending the possible applications of the superparamagnetic nanoparticles.

Data availability

The authors confirm that the relevant data backing the findings of the present study are available in the main article and the corresponding electronic ESI.† Raw data supporting the study are available from the corresponding author upon reasonable request.

Conflicts of interest

There are no conflicts to declare.

Acknowledgements

The author thanks Prof. S. Vasudevan for helpful discussions and for providing the facilities for executing this project.

Notes and references

1 R. J. Hamers, *Acc. Chem. Res.*, 2017, **50**, 633–637.
2 E. Kabir, V. Kumar, K. H. Kim, A. C. K. Yip and J. R. Sohn, *J. Environ. Manage.*, 2018, **225**, 261–271.
3 E. Asmatulu, M. N. Andalib, B. Subeshan and F. Abedin, *Environ. Chem. Lett.*, 2022, **20**, 2509–2529.
4 M. B. Mensah, J. A. M. Awudza and P. O'Brien, *R. Soc. Open Sci.*, 2018, **5**, 180824.
5 D. Wang, Q. Ma and P. Yang, *J. Nanosci. Nanotechnol.*, 2012, **12**, 6432–6438.
6 G. Cotin, C. Kiefer, F. Perton, D. Ihiawakrim, C. Blanco-Andujar, S. Moldovan, C. Lefevre, O. Ersen, B. Pichon, D. Mertz and S. Bégin-Colin, *Nanomaterials*, 2018, **8**, 881.
7 E. Wetterskog, M. Agthe, A. Mayence, J. Grins, D. Wang, S. Rana, A. Ahniyaz, G. Salazar-Alvarez and L. Bergström, *Sci. Technol. Adv. Mater.*, 2014, **15**, 055010.
8 M. B. Mensah, P. D. McNaughter, S. G. McAdams, F. Tuna, D. J. Lewis, J. A. M. Awudza, N. Revaprasadu and P. O'Brien, *ChemistrySelect*, 2018, **3**, 13548–13552.
9 J. W. M. Kyobe, E. B. Mubofu, Y. M. M. Makame, S. Mlowe and N. Revaprasadu, *Int. Nano Lett.*, 2016, **6**, 235–242.
10 E. B. Mubofu, *Sustainable Chem. Processes*, 2016, **4**, 1–12.
11 D. Gherca, A. Pui, N. Cornei, A. Cojocariu, V. Nica and O. Caltun, *J. Magn. Magn. Mater.*, 2012, **324**, 3906–3911.
12 R. L. de Paula and E. Frollini, *Biomass Convers. Biorefin.*, 2025, **15**, 4647–4656.
13 N. Salih, J. Salimon, B. M. Abdullah and E. Yousif, *Arab. J. Chem.*, 2017, **10**, S2273–S2280.
14 B. He, L. Zhou and J. Huang, *Mater. Lett.*, 2014, **117**, 142–145.
15 B. Meesaragandla, S. Sarkar, C. Hazra and V. Mahalingam, *Chempluschem*, 2013, **78**, 1338–1342.
16 M. Lattuada and T. A. Hatton, *Langmuir*, 2007, **23**, 2158–2168.
17 R. Hufschmid, H. Arami, R. M. Ferguson, M. Gonzales, E. Teeman, L. N. Brush, N. D. Browning and K. M. Krishnan, *Nanoscale*, 2015, **7**, 11142–11154.
18 Z. Chen, *Synth. React. Inorg., Met.–Org., Nano-Met. Chem.*, 2012, **42**, 1040–1046.
19 J. Park, K. An, Y. Hwang, J. E. G. Park, H. J. Noh, J. Y. Kim, J. H. Park, N. M. Hwang and T. Hyeon, *Nat. Mater.*, 2004, **3**, 891–895.
20 S. Reja, M. Kumar and S. Vasudevan, *Nanoscale Adv.*, 2024, **6**, 3857–3864.
21 M. Nahorniak, P. Pasetto, J. M. Greneche, V. Samaryk, S. Auguste, A. Rousseau, N. Nosova and S. Varvarenko, *Beilstein J. Nanotechnol.*, 2023, **14**, 11–22.
22 R. Chalasani and S. Vasudevan, *J. Phys. Chem. C*, 2011, **115**, 18088–18093.
23 M. M. Lin and D. K. Kim, *J. Nanoparticle Res.*, 2012, **14**, 688.
24 D. K. Kim and J. W. Lee, *J. Korean Ceram. Soc.*, 2018, **55**, 625–634.
25 R. Hufschmid, H. Arami, R. M. Ferguson, M. Gonzales, E. Teeman, L. N. Brush, N. D. Browning and K. M. Krishnan, *Nanoscale*, 2015, **7**, 11142–11154.
26 J. Park, K. An, Y. Hwang, J.-G. Park, H.-J. Noh, J.-Y. Kim, J.-H. Park, N.-M. Hwang and T. Hyeon, *Nat. Mater.*, 2004, **3**, 891–895.
27 C. Pereira, A. M. Pereira, C. Fernandes, M. Rocha, R. Mendes, M. P. Fernández-García, A. Guedes, P. B. Tavares, J.-M. Grenèche, J. P. Araújo and C. Freire, *Chem. Mater.*, 2012, **24**, 1496–1504.

28 S. Gyergyek, D. Pahovnik, E. Žagar, A. Mertelj, R. Kostanjšek, M. Beković, M. Jagodič, H. Hofmann and D. Makovec, *Beilstein J. Nanotechnol.*, 2018, **9**, 1613–1622.
29 B. H. Kim, N. Lee, H. Kim, K. An, Y. Il Park, Y. Choi, K. Shin, Y. Lee, S. G. Kwon, H. Bin Na, J.-G. Park, T.-Y. Ahn, Y.-W. Kim, W. K. Moon, S. H. Choi and T. Hyeon, *J. Am. Chem. Soc.*, 2011, **133**, 12624–12631.
30 A. Ullrich, M. M. Rahman, A. Azhar, M. Kühn and M. Albrecht, *J. Nanoparticle Res.*, 2022, **24**, 183.
31 Z. Soran-Erdem, V. K. Sharma, P. L. Hernandez-Martinez and H. V. Demir, *ACS Omega*, 2021, **6**, 20351–20360.
32 M. V. Kovalenko, M. I. Bodnarchuk, R. T. Lechner, G. Hesser, F. Schäffler and W. Heiss, *J. Am. Chem. Soc.*, 2007, **129**, 6352–6353.
33 S. Sun, H. Zeng, D. B. Robinson, S. Raoux, P. M. Rice, S. X. Wang and G. Li, *J. Am. Chem. Soc.*, 2004, **126**, 273–279.
34 N. Bao, L. Shen, Y. Wang, P. Padhan and A. Gupta, *J. Am. Chem. Soc.*, 2007, **129**, 12374–12375.
35 T. Dippong, E. A. Levei and O. Cadar, *Int. J. Mol. Sci.*, 2022, **23**, 8483.
36 S. M. Ansari, D. Phase, Y. D. Kolekar and C. V. Ramana, *Mater. Sci. Eng. B*, 2024, **300**, 117134.
37 R. Dou, H. Cheng, J. Ma and S. Komarneni, *Mater. Chem. Phys.*, 2020, **240**, 122181.
38 S. Reja and S. Vasudevan, *Nanoscale Adv.*, 2025, **7**, 329–335.